PAPER

Liposome biodistribution mapping with *in vivo* X-ray fluorescence imaging†

Giovanni Marco Saladino, [ID] *[a,b] Po-Han Chao, [ID] [b] Bertha Brodin, [ID] [a] Shyh-Dar Li [ID] [b] and Hans Martin Hertz [ID] [a]

Lipid-based nanoparticles are organic nanostructures constituted of phospholipids and cholesterol, displaying high *in vivo* biocompatibility. They have been demonstrated as effective nanocarriers for drug delivery and targeting. Mapping liposome distribution is crucial as it enables a precise understanding of delivery kinetics, tissue targeting efficiency, and potential off-target effects. Recently, ruthenium-encapsulated liposomes have shown potential for targeted drug delivery, photodynamic therapy, and optical fluorescence imaging. In the present work, we design $Ru(bpy)_3$-encapsulated liposomes (Ru-Lipo) empowering optical and X-ray fluorescence (XRF) properties for dual mode imaging and demonstrate the passivation role of liposomes over the free $Ru(bpy)_3$ compound. We employ whole-body XRF imaging to map the *in vivo* biodistribution of Ru-Lipo in mice, enabling tumor detection and longitudinal studies with elemental specificity and resolution down to the sub-millimeter scale. Quantitative XRF computed tomography on extracted organs permits targeting efficiency evaluations. These findings highlight the promising role of XRF imaging in pharmacokinetic studies and theranostic applications for the rapid optimization of drug delivery and assessment of targeting efficiency.

Introduction

Liposomes have been demonstrated to serve as efficient nanocarriers for drug delivery and targeting, with many products approved by the European Medicines Agency (EMA) and Food and Drug Administration (FDA).[1,2] The lipid bilayer structure of these nanoparticles mimics the natural cell membrane, facilitating interactions with biological systems. This feature enables encapsulation of a wide range of therapeutic agents, including hydrophobic and hydrophilic drugs, peptides, proteins, and nucleic acids.[3,4] Additionally, lipid-based nanoparticles can be modified with targeting ligands or surface modifications to enhance specific accumulation at desired sites, such as tumors or inflamed tissues, while minimizing off-target effects.[5] Furthermore, they can encapsulate various types of imaging agents, such as fluorescent dyes for optical imaging,[6–8] radionuclides for nuclear imaging,[9] or contrast agents for magnetic resonance imaging (MRI).[10,11] By loading the liposomes with two different types of imaging agents, they can enable dual mode imaging.[12,13]

Light-sensitive ruthenium(II) polypyridyl compounds represent powerful tools in photochemistry, recently emerging as potential prodrugs for photodynamic therapy (PDT),[14–16] which employs visible and near-infrared light for cancer treatment enabling precise spatial and temporal control over the cytotoxicity, thus reducing adverse effects in cancer patients.[17] In this context, sterically hindered liposomes, including a polyethylene glycol (PEG) capping, can be employed as versatile and biocompatible contrast agents and drug carriers for treating various diseases owing to their prolonged circulation time in the bloodstream.[18,19]

Recently, X-ray fluorescence (XRF) has been applied for *in vivo* imaging of small animals with high resolution and elemental specificity, using a laboratory setup.[20] This has been achieved through the design of inorganic nanoparticles (NPs) as contrast agents, consisting of elements such as molybdenum (Mo), ruthenium (Ru), or rhodium (Rh), whose absorption edge aligns with the energy of the X-ray source (24 keV).[21–23] Nevertheless, the highly crystalline nature of inorganic NPs has recently brought concerns over long-term toxicity, due to low dissolution rates, high residence times, and undesired accumulations.[24,25]

In the present work, we design liposomes encapsulating a ruthenium(II) polypyridyl compound, which can function alone as a dual mode imaging agent, enabling both XRF and optical fluorescence imaging. Owing to its properties, we map the liposome biodistribution *in vivo* with longitudinal studies

[a]Department of Applied Physics, Bio-Opto-Nano Physics, KTH Royal Institute of Technology, SE 10691 Stockholm, Sweden. E-mail: saladino@kth.se
[b]Faculty of Pharmaceutical Sciences, University of British Columbia, V6T 1Z3 Vancouver, British Columbia, Canada
†Electronic supplementary information (ESI) available. See DOI: https://doi.org/10.1039/d4nr02793k

using both the imaging modalities, achieving passive tumor targeting. The results evidence that the high penetration depth, high resolution, and elemental specificity of XRF imaging enable the rapid and accurate evaluation of the Ru-Lipo biodistribution *in vivo* and their quantification in extracted organs. The generality of the synthesis method and the ruthenium-specific detectability with XRF pave the way to theranostic application using PDT-specific ruthenium(II) poly-pyridyl compounds.

Results and discussion

Methodology

We conceptually illustrated the enabled dual-mode *in vivo* imaging methodology with optical fluorescence and XRF (Fig. 1). PEGylated Ru-Lipo were designed to empower both optical fluorescence and XRF properties, exploiting the intrinsic adsorption edge of ruthenium as the XRF contrast agent and the optical fluorescence properties of the organic dye, Ru(bpy)$_3$ (Fig. 1a). After assessing the viability *in vitro*, Ru-Lipo could be employed as dual-mode contrast agents, intravenously injected into mice. Biodistribution and pharmacokinetics or Ru-Lipo could be investigated with projection images obtained *via* optical fluorescence and XRF imaging. Optical fluorescence imaging was achieved by employing a commercial *in vivo* imaging system (IVIS), by matching the excitation (465 nm) and emission (620 nm) windows with the optical fluorescence characteristics of Ru(bpy)$_3$ (Fig. 1b).

A schematic representation of the *in vivo* XRF imaging arrangement (Fig. 1c) highlighted the employment of a monochromatic X-ray pencil beam (24 keV), generating XRF radiation when exciting a contrast agent constituted of an element (Ru) with its adsorption edge (K_{Ru} = 22 keV) matching the X-ray source energy. The transmitted radiation could be employed for conventional X-ray (transmission) imaging to be overlaid by the XRF signal. A movable stage, monitoring and anesthesia equipment enabled *in vivo* imaging of mice in scanning mode, with a resolution of down to 100 μm (spot size).[20]
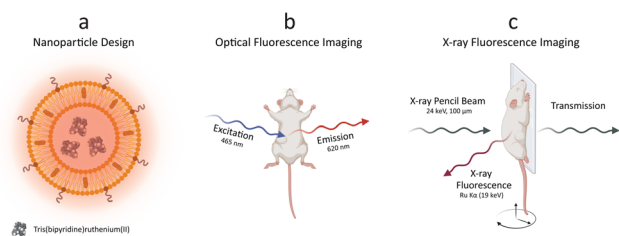
Contrast agent design

The Ru-Lipo formulation was prepared through hydration of lipid thin-films, followed by membrane extrusion to control the size, dialysis against saline to remove the unencapsulated contrast agent, and concentrated with centrifuge filters (Fig. S1†). The physical characteristics of Ru-Lipo were studied, including morphological analysis, hydrodynamic size and ζ-potential (Fig. 2). Cryo-TEM micrographs of Ru-Lipo evidenced a uniform spherical morphology (Fig. 2a) and an intact lipidic bilayer membrane (Fig. S2a†) with an estimated diameter of 88 ± 29 nm (Fig. S2b†).

The hydrodynamic size distribution highlighted a nearly monodisperse sample with an intensity peak at 87 nm, with a polydispersity index (PDI) of 0.03, indicating a uniform particle population (Fig. S3a†), consistent with the results obtained by electron microscopy. A longitudinal study conducted at 37 °C over a period of 3 days highlighted the stability of the synthesized Ru-Lipo, with negligible variations of the hydrodynamic size (Fig. S3b†). After 72 h, the release of Ru(bpy)$_3$ was estimated to be 6.4 ± 0.1%, as determined by optical spectroscopy. The hydrodynamic size was followed over the three synthesis steps, showing no significant changes between extrusion and ultrafiltration steps (Fig. 2b). The ζ-potential of Ru-Lipo, indicating their surface charge, was estimated as −29 ± 9 mV, indicating a negative charge in water, at pH 6.5 (Fig. 2c), typical for liposomes PEGylated with 1,2-distearoyl-*sn-glycero*-3-phosphoethanolamine-*N*-[methoxy(polyethyleneglycol)-2000] (DSPE-PEG), which do not shield the entire surface charge, thus leading to negatively charged sterically stabilized liposomes.[26]

Owing to its dual-mode properties, the Ru-Lipo formulation was also measured for Ru content by means of optical and X-ray fluorescence (Fig. 3). By exposing several Ru-Lipo dilutions to the X-ray pencil beam of a liquid metal-jet X-ray source (24 keV),[20] the XRF signal from Ru Kα and Ru Kβ emission peaks could be recorded and collected by photon-counting silicon-drift detectors (Fig. 3a). Furthermore, Thomson scattering (λ_T) and Compton scattering (λ_C) could be identified, and the latter's contributions subtracted as the background from the XRF signal (Fig. S4a†). The Ru Kα emission peaks

Fig. 1 Dual mode imaging with ruthenium-encapsulated liposomes. Schematic illustration of (a) the nanoparticle design, (b) optical fluorescence imaging, and (c) X-ray fluorescence imaging. PEGylated liposomes were synthesized with the thin-film hydration method, encapsulating a hydrophilic ruthenium dye. Optical fluorescence imaging was performed with a commercial *in vivo* imaging system (IVIS), while X-ray fluorescence imaging was achieved with a laboratory liquid-metal jet X-ray source.
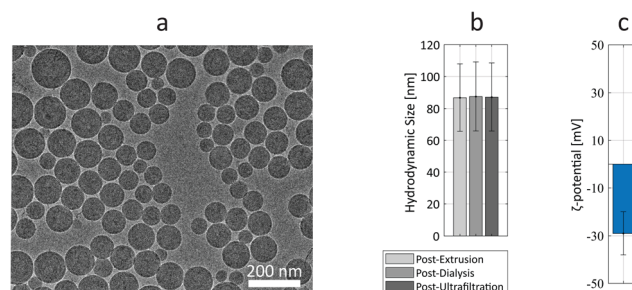

Fig. 2 Nanoparticle characterization. (a) Cryo-TEM micrograph of ruthenium-encapsulated liposomes, Ru-Lipo. Scale bar, 200 nm. (b) Average hydrodynamic size values in saline solution (0.9%) after each synthesis step. (c) ζ-Potential of Ru-Lipo in water (pH 6.5).
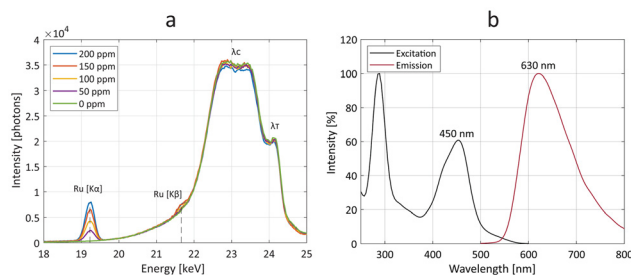
Fig. 3 Optical and X-ray fluorescence properties. (a) X-ray fluorescence spectra of stock solutions with several concentrations of ruthenium-encapsulated liposomes (Ru-Lipo), highlighting the Ru Kα and Ru Kβ emission peaks. Compton (λ_C) and Thomson (λ_T) scattering are also indicated. (b) Excitation (black) and emission (red) optical fluorescence spectra of Ru-Lipo, evidencing the excitation and emission peaks in the visible range, at 450 nm and 630 nm, respectively.

were employed for quantitative estimations (Fig. S4b†) and subsequent XRF imaging. Besides the XRF properties, Ru-Lipo exhibited the same optical fluorescence emission profile as the free Ru(bpy)$_3$ (Fig. S5a†). The excitation and emission spectra highlighted intensity peaks in the visible range, at 450 nm and 630 nm, respectively (Fig. 3b). Furthermore, the addition of Triton X 10% to a diluted dispersion of Ru-Lipo was used for liposome's membrane disruption[27] and led to a variation in the sample's optical fluorescence of 2%, which was ascribed to random errors and solvent evaporation. Hence, the encapsulation of Ru(bpy)$_3$ in the liposome core did not lead to fluorescence quenching effects due to potentially limited hydrated environment. For this reason, optical fluorescence could be used for the quantitative estimations of encapsulation efficiency (EE) and Ru(bpy)$_3$ concentration.

A calibration curve was obtained for Ru(bpy)$_3$ concentration values of up to 40 μM, by a linear fit (Fig. S5b†). The EE and Ru-to-lipid weight ratio, 10% and 1.8% respectively (Table S1†), were in line with other formulations prepared with 1,2-distearoyl-*sn-glycero*-3-phosphatidylcholine (DSPC) and hydrophilic loads.[28] DSPC was chosen as the main lipid component for yielding liposomes empowering slow load release, long circulation times, and high tumoral delivery, compared to other phospholipids.[28] The PEGylation introduced through DSPE-PEG enhances liposome stability *in vivo*, by limiting opsonization and absorption by the reticuloendothelial system.[29] The constituents of the Ru-Lipo formulation were investigated with Fourier-transform infrared spectroscopy (FT-IR) and ultra-performance liquid chromatography (UPLC). All the FT-IR spectra (Fig. S6a†) of the lipidic components exhibited the typical lipidic backbone bands, including $\delta_s(CH_2)$ at 1468 cm^{-1}, $\nu_s(CH_2)$ at 2850 cm^{-1}, and $\nu_{as}(CH_2)$ at 2916 cm^{-1}.[30] The C=O stretching vibration for DSPC was associated with the band at 1728 cm^{-1},[31] while the band at 772 cm^{-1} was ascribed to the bipyridine ring breathing of Ru(bpy)$_3$.[32] The UPLC analysis (Fig. S6b†) evidenced the presence of all the three lipidic components in Ru-Lipo, DSPC, cholesterol, and DSPE-PEG. Furthermore, it permitted to estimate

the effective lipid ratio (Table S1†), highlighting DSPC as the limiting lipidic component for the final formulation. The Ru-to-lipid weight ratio was hereby limited by the solubility of the compound. In future endeavors, the Ru-to-lipid weight ratio could be increased through the implementation of solvent-assisted active loading mechanisms.[33] This approach would enhance the relative concentration of the XRF-active element (Ru). Consequently, it would be possible to achieve higher sensitivity with XRF imaging. Furthermore, the replacement of Ru(bpy)$_3$ with Ru-containing photosensitizers for phototherapy applications, including compounds currently under evaluation in clinical trials,[34–36] can enable the development of theranostic nanoparticles.

Biocompatibility

The synthesized Ru-Lipo were tested *in vitro* using a real-time cell analysis (RTCA) assay to assess their role in ameliorating the toxicity of the free dye, Ru(bpy)$_3$. RTCA enabled longitudinal studies, by measuring the cell proliferation over time of murine macrophages (Fig. 4). This cell line (RAW 264.7) was selected for *in vitro* toxicity evaluations owing to the macrophage's role in the immune response of external stimuli, including nanoparticles, leading to nanoparticle uptake and sequestration in liver and spleen.[37–39] Furthermore, in our previous studies, macrophages consistently exhibited a strong concentration-dependent response,[22,40] making them the preferred choice for assessing nanoparticle cytotoxicity prior to *in vivo* studies.

Cells exposed to a low concentration (50 ppm) did not evidence any significant difference between Ru-Lipo and the free dye, Ru(bpy)$_3$ (Fig. S7a†). Both the higher tested ruthenium concentrations (100 and 200 ppm) highlighted a significant passivation role of the liposomes (Fig. 4), with Ru-Lipo and Ru(bpy)$_3$ leading to a concentration- and time-dependent viability. The free dye exhibited a half-maximal inhibitory concentration (IC$_{50}$) of 200 ppm at 48 h, while Ru-Lipo did not show any significant difference in cell index compared to unexposed control cells, during the proliferation phase ($t < 60$ h), at the tested concentrations and exposure times. By comparing the
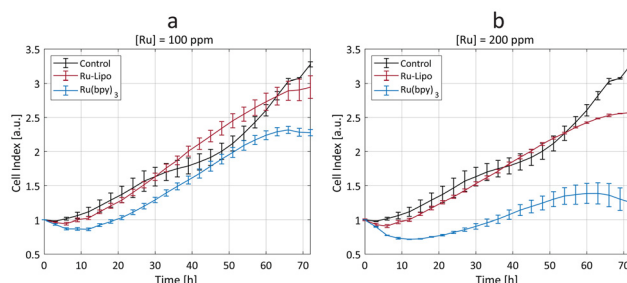

Fig. 4 Cytotoxicity study. Real-time cell analysis (RTCA) assay on macrophages (RAW 264.7), after exposure to ruthenium-encapsulated liposomes (Ru-Lipo, in red) and free ruthenium dye, Ru(bpy)$_3$ (in blue) with two ruthenium concentrations, (a) 100 ppm and (b) 200 ppm. The cell index values are compared to unexposed (negative) control cells (black). Measurements were made in triplicates ($\pm$SD).

same ruthenium concentrations in form of free and encapsulated dye, it was possible to validate the beneficial role of employing liposomes as the carriers for XRF contrast agents, as a possible alternative to inorganic passivation strategies, such as silica shell coating or conjugation with carbon quantum dots.[21,41] Finally, live imaging of cells exposed to Ru-Lipo demonstrated the possibility to track and visualize the liposomes *in vitro* (Fig. S7b†), by means of their optical fluorescence properties (Fig. S5a†).

Preclinical imaging

Owing to the dual fluorescence properties of the designed contrast agents, Ru-Lipo could be employed both for XRF and optical fluorescence imaging. Mice injected with Ru-Lipo were imaged *in vivo* employing the laboratory liquid-metal jet X-ray source or a commercial optical fluorescence imaging system (Fig. 5). *In vivo* XRF projection images highlighted a specific biodistribution pattern, by detecting Ru Kα emission photons and overlaying them on the simultaneously acquired X-ray transmission image (Fig. 5a).

Longitudinal scans on the same mice at several time points (1 h, 5 h, and 24 h) permitted to identify the optimal time interval between injection and imaging for tumor detection (Fig. S8†). At early stages (1 h and 5 h), Ru-Lipo exhibited a scattered biodistribution, including detection from the lungs, liver, and spleen, indicating long circulation times. Finally, Ru-Lipo accumulated mainly in spleen, liver, and xenografted tumor, 24 h after injection.

The passive tumor targeting was confirmed with the IVIS system, exploiting the optical fluorescence properties of Ru-Lipo (Fig. 5b). The organ distribution study with optical fluorescence was hindered by the limited penetration depth and tissue autofluorescence in the optical spectrum (Fig. S9†), which only permits the signal detection up to a few millimeters beneath the skin surface.[42,43] These results supported the possibility to perform dual-mode imaging solely employing the intrinsic properties of Ru(bpy)$_3$ together with the passivating and capping functions of liposomes to achieve biocompatible and sufficiently confined contrast agents. Liver and spleen

retention of intravenously injected nanoparticles by resident macrophages is a common and undesired outcome.[44,45] Nanoparticle sequestration can be limited by inducing a temporary macrophage depletion or by introducing specific surface functionalization to minimize opsonization.[46] In the present work, PEGylation likely shielded the liposome surface from fast opsonization and phagocytosis by the mononuclear phagocytic system. For this reason, Ru-Lipo reduced the previously encountered undesired accumulations in the liver, when employing inorganic contrast agents, enabling tumor detection without macrophage depletion.[40,47] In the future, improved tumor detection could be achieved by refining the Ru-Lipo design aiming at increasing the Ru-to-Lipid ratio, thus enabling higher injection doses.

Inorganic Ru NPs are known to have slow dissolution rates even in acids, often requiring microwave digestion processing.[48] Furthermore, recent *in vivo* studies employing Ru NPs as XRF contrast agents highlighted long residence times with accumulations in liver, spleen, and skin persisting for over two weeks, after intravenous administration.[25] On the other hand, PEGylated liposomes possess a half-life of up to 45 h,[49] and their cargo loading undergoes rapid renal excretion after liposome degradation.[29,50] For this reason, the designed Ru-Lipo constitute a new generation of XRF contrast agents.

The efficacy, safety, and overall therapeutic potential of nanomedicines are largely determined by their biodistribution profiles.[51,52] Therefore, quantitative analysis of nanoparticle distribution in organs is crucial for the design and development of effective nanomedicines. The main organs affected by liposome accumulations and tumor were excised, extracted, and scanned *ex vivo* with the XRF imaging setup (Fig. 6).

XRF computed tomography (XFCT) has been demonstrated to provide reliable quantitative estimations, previously validated with inductively coupled plasma (ICP) mass spectrometry.[53] In the present work, the tomographic reconstructions highlight a homogenous distribution of Ru-Lipo in liver, spleen, and kidneys (Fig. 6a). The successful passive targeting of Ru-Lipo to xenografted tumors was confirmed with XFCT,
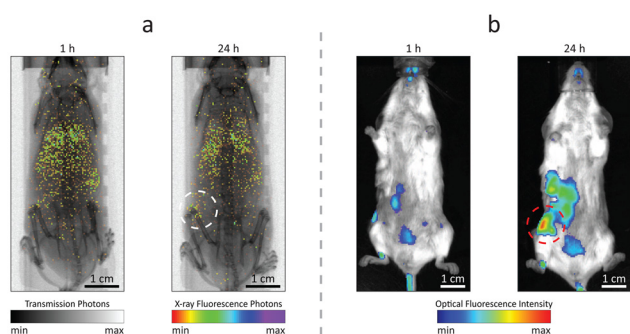

Fig. 5 Dual mode imaging. *In vivo* (a) X-ray fluorescence projection images and (b) optical fluorescence imaging of mice, 1 h and 24 h after injection with ruthenium-encapsulated liposomes (Ru-Lipo). The tumor area is highlighted with dashed circles. Scale bars, 1 cm.
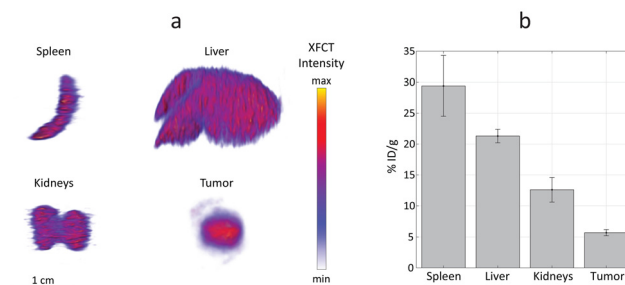

Fig. 6 Quantitative accumulation estimation. (a) X-ray fluorescence computed tomography (XFCT) of spleen, liver, kidneys, and tumors, extracted from mice injected with ruthenium-encapsulated liposomes (Ru-Lipo). (b) Quantitative estimation of Ru-Lipo uptake in specific organs and tumors *via* XFCT, normalized to tissue weight and injected dose (% ID per g, ±SD). Scale bar, 1 cm.

evidencing the highest local Ru concentration in the tumor core.

Typically, ICP techniques are employed for quantitative studies in nanomedicine, particularly for determining nanoparticle distribution in organs.[54,55] However, these methods often lead to extended processing times, which can be a significant drawback in time-sensitive research and applications. Furthermore, the ICP-analyzed sample usually consists of only a small acid-digested portion of the overall organ, which may result in partial or biased information about the nanoparticle distribution. XFCT allowed to obtain a 3D distribution map leading to an average estimation of the overall Ru-Lipo accumulation in the organs and tumor (Fig. 6b), providing a more comprehensive and representative analysis of nanoparticle distribution.

The quantitative nanoparticle distribution analysis demonstrated that the spleen was responsible for the highest liposome sequestration normalized by organ weight (29 ± 5% ID per g), followed by liver (21 ± 1% ID per g) and kidneys (13 ± 2% ID per g). In fact, nanoparticle sequestration by the liver resident macrophages (Kupffer cells) and splenic macrophages is well documented.[37,38] The minimal accumulations in kidneys were attributed to the choice of DSPC, as the main lipidic component of Ru-Lipo, which can lower the risk of nephrotoxicity.[28] The limited variability among different samples highlights the reliability of this methodology for quantitatively estimating nanoparticle distribution in organs. We speculate that undetected Ru-Lipo were either excreted within the first 24 hours or were still in circulation, below the detection limit.[22] Overall, this strategy for liposome design enabled *in vivo* tumor detection *via* XRF imaging with a single administration of Ru-Lipo, registering a tumor delivery efficiency of 5.7 ± 0.5% ID per g, consistent with existing literature.[55]

Conclusions

In the present work, we introduced a methodology for biodistribution studies of ruthenium-encapsulated liposomes using XRF imaging. The same XRF imaging setup used for *in vivo* image acquisition was also used for the quantitative analysis of nanoparticles in organs. This not only streamlined the process, but also ensured consistency between the imaging and analysis stages, leading to more rapid and reliable results. Dual mode imaging with optical and XRF fluorescence validated the passive targeting of tumors. Moreover, the transition from inorganic to organic nanoparticles as the XRF contrast agents enabled tumor detection without the need of macrophage depletion. Furthermore, the wider availability of FDA-approved liposomal formulations enhances the possible applications of XRF imaging in pharmaceutical and medical research. In the future, the careful choice of specific ruthenium(II) polypyridyl compounds with therapeutic action will confer the possibility to develop theranostic nanoparticles,

owing to the elemental specificity of XRF imaging for ruthenium.

Experimental

Materials

1,2-Distearoyl-*sn*-glycero-3-phosphatidylcholine (DSPC) and 1,2-distearoyl-*sn*-glycero-3-phosphoethanolamine-*N*-[methoxy(polyethyleneglycol)-2000] (DSPE-PEG) were purchased from Avanti Polar Lipids (Alabaster, AL). Cholesterol (CH), tris(2,2-bipyridyl)dichlororuthenium(II) hexahydrate (Ru(bpy)$_3$), and Triton X 10% were obtained from Sigma Aldrich. All other reagents were of analytical grade.

Liposome preparation

The lipid components (DSPC, CH and DSPE-PEG) were mixed in chloroform at a mole ratio of 56.4 : 38.3 : 5.3, for a total of 60 mg. Solvent was evaporated at 50 °C with Rotavapor. The thin film was then hydrated with an aqueous solution of Ru(bpy)$_3$ (1 mL, 0.1 mmol in saline solution 0.9%) at 50 °C, to form multi-lamellar vesicles (MLVs). MLVs were extruded 21 times through polycarbonate filters (Nuclepore Track-Etch Membranes, Whatman) of 0.2 μm pore size first, and then repeated with 0.1 μm pore size, each at 65 °C, to adjust liposome size to around 100 nm. Formulations were then transferred to a dialysis tube (Biosciences Pur-A-Lyzer Midi Dialysis Kit 12 kDa MWCO, Sigma Aldrich, SE) and dialyzed against saline (500 mL) for 0.5 h. Saline was changed and dialyzed again for 1 h, and then overnight. Finally, the formulation was concentrated with centrifuge filter units (Amicon® Ultra Centrifugal Filter, 30 kDa MWCO) (Fig. S1†). Empty liposomes were synthesized following the same steps, without the addition of Ru(bpy)$_3$.

Liposome characterization

The size and zeta potential of the liposomes were measured by dynamic light scattering (DLS) with a Zetasizer Nano (Malvern Instruments Ltd, United Kingdom). Cryogenic transmission electron microscopy (Krios G3i Cryo-TEM, Thermo Fisher Scientific, Sweden) was employed for the morphological characterization of Ru-Lipo. Ultraviolet-visible spectrophotometry (UV-vis, NP80, Implen) was employed to estimate the load release percentage after incubation in saline solution (0.9%) at 37 °C for 72 h. The filtrate was collected using a centrifuge filter unit and the optical absorption at 430 nm was compared to known amounts of Ru(bpy)$_3$. Liposome disruption studies were performed with Triton X 10%.[27] The structural characterization was investigated with FT-IR (PerkinElmer, USA) and Acquity UPLC chromatography system (Waters, USA). The concentration was confirmed with XRF spectrum acquisitions of the Ru-Lipo stocks by obtaining a calibration curve using several dilutions of Ru standards (Fig. S4b†).[20] The X-ray spectra were acquired with scans of 180 s. Optical fluorescence measurements were obtained with the Synergy Mx Monochromator-Based Multi-Mode Microplate

Reader (BioTek, VT, USA). The encapsulation efficiency (EE) was determined as $[Ru]_L/[Ru]_0 \times 100\%$, where $[Ru]_L$ is the concentration of Ru in the liposome, and $[Ru]_0$ is the concentration of the hydration solution.

Cell studies

The real-time cell analysis assay (xCELLigence Agilent, St Clara, USA) was used to demonstrate the passivation role of the encapsulating liposomes (Ru-Lipo) over the free dye – Ru (bpy)$_3$. The assay was performed on RAW 264.7 (ATCC-TIB-71) cell line, at two Ru concentrations (200 and 100 ppm) in triplicates (96-well plate, biological replicates, ±SD). Untreated cells were the negative control. The estimated viability was based on the quantification of the impedance, an indicator of cell proliferation. The cells were allowed to adhere to the plate surface for 24 hours before exposure to the compound (time = 0). Live images of the cells were obtained using an EVOS 5000 Imaging System (Thermo Fisher Scientific, MA, USA).

Animal studies

Experiments with mice were approved by the regional animal ethics committee of Northern Stockholm, Sweden (ethical permit number 13156-2022), according to institutional, national, and European guidelines for animal handling and research (L150/SJVFS 2019:9 and 2010/63/EU) or following the protocol (A22-0141) approved by the Animal Care Committee of the University of British Columbia (Vancouver, BC, Canada). Eight-week-old female albino mice (BALB/c) were obtained from Janvier Labs (France) or Charles River Laboratories (Wilmington, USA) and housed under controlled temperature (21 ± 1 °C) and humidity ($55 \pm 5\%$) conditions, with light–dark cycle and *ad libitum* feeding. The general conditions of the mice were assessed before and during the study, checking for possible onsets of behavioural and/or morphological changes. 6 mice were xenografted with the syngeneic breast adenocarcinoma cell line 4T1 by subcutaneously injecting $\approx 10^6$ cells suspended in phosphate-buffered saline (PBS, 100 μL). After 1 week, the xenografted mice were intravenously injected with Ru-Lipo formulations (100 μL, 10 mg$_{Ru}$ kg^{-1}). Mice were imaged with either optical fluorescence or XRF imaging arrangements.

X-ray fluorescence imaging

Whole-body XRF projection images were acquired *in vivo* with our laboratory liquid-metal jet X-ray source for XRF imaging.[56] XRF scans were performed under anesthesia with isoflurane (Abbott, Sweden) at several time points (1 h, 5 h, and 24 h). During the imaging sessions, ophthalmic ointment (Oculentum simplex, APL, Sweden) was applied to the eyes for cornea protection; temperature and respiration were also monitored. A step size of 200 μm and exposure time of 10 ms per step were chosen, resulting in a 15 min scanning time. A binning factor of 2 was used for XRF imaging. The average radiation dose was equal to 1 mGy for a whole-body projection image.[57] XFCT was acquired for extracted and fixed tissues using a voxel size of $200 \times 200 \times 200$ μm^3, acquiring 30 projec-

tions over 180°, with an exposure time of 25 ms per step, resulting into scanning times ranging from about 1 h for spleen, tumor, and kidneys to up to 3.5 h for the liver.

Optical fluorescence imaging

Anesthetized mice were imaged using an IVIS® Imaging System (Caliper Life Sciences, Waltham, MA, USA) at several time points (1 h, 5 h, and 24 h). For the acquisition, the exposure time was set to 30 s and a binning factor of 4 was used. The employed excitation and emission filters were 465 nm and 620 nm, respectively, to match the optical fluorescence properties of Ru(bpy)$_3$.

Author contributions

Conceptualization, methodology, formal analysis, data curation, software, writing—original draft, and visualization: G. M. S. Investigation: G. M. S., P. C., and B. B. Writing—review and editing: G. M. S., P. C., B. B., S. L., and H. M. H. Supervision and resources: S. L. and H. M. H.

Data availability

The data supporting this article have been included as part of the ESI.†

Conflicts of interest

There are no conflicts to declare.

Acknowledgements

References

1 R. K. Thapa and J. O. Kim, *J. Pharm. Invest.*, 2023, **53**, 19.

2 S. Giordani, V. Marassi, A. Zattoni, B. Roda and P. Reschiglian, *J. Pharm. Biomed. Anal.*, 2023, **236**, 115751.

3 S. H. Crayton, A. K. Chen, J. F. Liu, E. M. Higbee-Dempsey, C. H. Huang, A. Tsourkas and Z. Cheng, *Comprehensive Biomaterials II*, 2017, p. 424.

4 C. Wang, X. Lan, L. Zhu, Y. Wang, X. Gao, J. Li, H. Tian, Z. Liang and W. Xu, *Small*, 2024, 2309031.

5 M. J. Mitchell, M. M. Billingsley, R. M. Haley, M. E. Wechsler, N. A. Peppas and R. Langer, *Nat. Rev. Drug Discovery*, 2020, **20**, 101.

6 V. Deissler, R. Rüger, W. Frank, A. Fahr, W. A. Kaiser and I. Hilger, *Small*, 2008, **4**, 1240.

7 K. N. Tasnim, A. Rahman, S. M. Newaj, O. Mahmud, S. Monira, T. Z. Khan, H. M. Reza, M. Shin and S. Md. Sharker, *ACS Appl. Bio Mater.*, 2024, **7**(5), 3190.

8 Y. Bian, Y. Zhang, B. Hu, Y. Huang, W. Liang, Q. Yuan, J. Zhang, X. Gao, D. Su, Y. Bian, W. Liang, Q. Yuan, X. Gao, D. Su, Y. Zhang and J. Zhang, *Small*, 2024, 2401282.

9 F. Man, P. J. Gawne and R. T. M. de Rosales, *Adv. Drug Delivery Rev.*, 2019, **143**, 134.

10 W. J. M. Mulder, G. J. Strijkers, A. W. Griffioen, L. Van Bloois, G. Molema, G. Storm, G. A. Koning and K. Nicolay, *Bioconjugate Chem.*, 2004, **15**, 799.

11 P. Šimečková, F. Hubatka, J. Kotouček, P. Turánek Knötigová, J. Mašek, J. Slavík, O. Kováč, J. Neča, P. Kulich, D. Hrebík, J. Stráská, K. Pěnčíková, J. Procházková, P. Diviš, S. Macaulay, R. Mikulík, M. Raška, M. Machala and J. Turánek, *Sci. Rep.*, 2020, **10**, 1.

12 A. de Vries, M. B. Kok, H. M. H. F. Sanders, K. Nicolay, G. J. Strijkers and H. Grüll, *Contrast Media Mol. Imaging*, 2012, **7**, 68.

13 M. K. Ravoori, S. Singh, R. Bhavane, A. K. Sood, B. Anvari, J. Bankson, A. Annapragada and V. Kundra, *Sci. Rep.*, 2016, **6**, 1.

14 J. Karges, S. Kuang, F. Maschietto, O. Blacque, I. Ciofini, H. Chao and G. Gasser, *Nat. Commun.*, 2020, **11**, 1.

15 L. Conti, E. Macedi, C. Giorgi, B. Valtancoli and V. Fusi, *Coord. Chem. Rev.*, 2022, **469**, 214656.

16 C. Parella, A. Blanquer, S. Sinha, E. Hümpfner, J. Hernando, E. Mora, X. Fontrodona, Z. Kelemen, C. Nogués, R. Núñez and I. Romero, *Dyes Pigm.*, 2024, **224**, 111985.

17 X. Li, J. F. Lovell, J. Yoon and X. Chen, *Nat. Rev. Clin. Oncol.*, 2020, **17**, 657.

18 E. Blanco, H. Shen and M. Ferrari, *Nat. Biotechnol.*, 2015, **33**, 941.

19 D. Gao, Z. Luo, Y. He, L. Yang, D. Hu, Y. Liang, H. Zheng, X. Liu and Z. Sheng, *Small*, 2023, **19**, 2206544.

20 K. G. Y. Arsana, G. M. Saladino, B. Brodin, M. S. Toprak and H. M. Hertz, *Int. J. Mol. Sci.*, 2024, **25**, 920.

21 G. M. Saladino, C. Vogt, Y. Li, K. Shaker, B. Brodin, M. Svenda, H. M. Hertz and M. S. Toprak, *ACS Nano*, 2021, **15**(3), 5077.

22 G. M. Saladino, C. Vogt, B. Brodin, K. Shaker, N. I. Kilic, K. Andersson, M. Arsenian-Henriksson, M. S. Toprak and H. M. Hertz, *Nanoscale*, 2022, **15**, 2214.

23 N. I. Kilic, G. M. Saladino, S. Johansson, R. Shen, C. McDorman, M. S. Toprak and S. Johansson, *ACS Appl. Mater. Interfaces*, 2023, **15**, 49794.

24 R. Mohammapdour and H. Ghandehari, *Adv. Drug Delivery Rev.*, 2022, **180**, 114022.

25 C. Vogt, G. M. Saladino, K. Shaker, M. Arsenian-Henriksson, H. M. Hertz, M. S. Toprak and B. A. Brodin, *Nanomedicine*, 2023, **18**(18), 1161.

26 M. Petrini, W. J. M. Lokerse, A. Mach, M. Hossann, O. M. Merkel and L. H. Lindner, *Int. J. Nanomed.*, 2021, **16**, 4045.

27 J. R. Jimah, P. H. Schlesinger and N. H. Tolia, *Bio-Protoc.*, 2017, 7(15), e2433.

28 Y. Zhao, J. P. May, I. W. Chen, E. Undzys and S. D. Li, *Pharm. Res.*, 2015, **32**, 3261.

29 S. Paramshetti, M. Angolkar, S. Talath, R. A. M. Osmani, A. Spandana, A. Al Fatease, U. Hani, K. V. R. N. S. Ramesh and E. Singh, *Life Sci.*, 2024, **346**, 122616.

30 A. R. Caldas, J. Catita, R. Machado, A. Ribeiro, F. Cerqueira, B. Horta, R. Medeiros, M. Lúcio and C. M. Lopes, *Pharmaceutics*, 2021, **13**, 1202.

31 B. Kästner, C. M. Johnson, P. Hermann, M. Kruskopf, K. Pierz, A. Hoehl, A. Hornemann, G. Ulrich, J. Fehmel, P. Patoka, E. Rühl and G. Ulm, *ACS Omega*, 2018, **3**, 4141.

32 M. U. Munshi, J. Martens, G. Berden and J. Oomens, *J. Phys. Chem. A*, 2020, **124**, 2449.

33 W. L. Tang, W. H. Tang, A. Szeitz, J. Kulkarni, P. Cullis and S. D. Li, *Biomaterials*, 2018, **166**, 13.

34 S. Monro, K. L. Colón, H. Yin, J. Roque, P. Konda, S. Gujar, R. P. Thummel, L. Lilge, C. G. Cameron and S. A. McFarland, *Chem. Rev.*, 2019, **119**, 797.

35 S. A. McFarland, A. Mandel, R. Dumoulin-White and G. Gasser, *Curr. Opin. Chem. Biol.*, 2020, **56**, 23.

36 M. Ankathatti Munegowda, A. Manalac, M. Weersink, S. A. McFarland and L. Lilge, *Coord. Chem. Rev.*, 2022, **470**, 214712.

37 S. Wilhelm, A. J. Tavares, Q. Dai, S. Ohta, J. Audet, H. F. Dvorak and W. C. W. Chan, *Nat. Rev. Mater.*, 2016, **1**, 16014.

38 W. Ngo, S. Ahmed, C. Blackadar, B. Bussin, Q. Ji, S. M. Mladjenovic, Z. Sepahi and W. C. W. Chan, *Adv. Drug Delivery Rev.*, 2022, **185**, 114238.

39 T. Anchordoquy, N. Artzi, I. V. Balyasnikova, Y. Barenholz, N. M. La-Beck, J. S. Brenner, W. C. W. Chan, P. Decuzzi, A. A. Exner, A. Gabizon, B. Godin, S. K. Lai, T. Lammers, M. J. Mitchell, S. M. Moghimi, V. R. Muzykantov, D. Peer, J. Nguyen, R. Popovtzer, M. Ricco, N. J. Serkova, R. Singh, A. Schroeder, A. A. Schwendeman, J. P. Straehla, T. Teesalu, S. Tilden and D. Simberg, *ACS Nano*, 2024, **18**, 13983.

40 G. M. Saladino, B. Brodin, R. Kakadiya, M. S. Toprak and H. M. Hertz, *Sci. Adv.*, 2024, **10**, eadl2267.

41 G. M. Saladino, N. I. Kilic, B. Brodin, B. Hamawandi, I. Yazgan, H. M. Hertz and M. S. Toprak, *Nanomaterials*, 2021, **11**(9), 2165.

42 X. Meng, F. Yang, H. Dong, L. Dou and X. Zhang, *Nano Today*, 2021, **38**, 101156.

43 L. Finlayson, I. R. M. Barnard, L. McMillan, S. H. Ibbotson, C. T. A. Brown, E. Eadie and K. Wood, *Photochem. Photobiol.*, 2022, **98**, 974.

44 Y. N. Zhang, W. Poon, A. J. Tavares, I. D. McGilvray and W. C. W. Chan, *J. Controlled Release*, 2016, **240**, 332.

45 W. Poon, Y. N. Zhang, B. Ouyang, B. R. Kingston, J. L. Y. Wu, S. Wilhelm and W. C. W. Chan, *ACS Nano*, 2019, **13**, 5785.

46 J. S. Suk, Q. Xu, N. Kim, J. Hanes and L. M. Ensign, *Adv. Drug Delivery Rev.*, 2016, **99**, 28.

47 E. Samuelsson, H. Shen, E. Blanco, M. Ferrari and J. Wolfram, *Colloids Surf., B*, 2017, **158**, 356.

48 Y. Yang, C. Sun, Y. Ren, S. Hao and D. Jiang, *Sci. Rep.*, 2014, **4**, 4540.

49 J. Heyes, K. Hall, V. Tailor, R. Lenz and I. MacLachlan, *J. Controlled Release*, 2006, **112**, 280.

50 S. Ait-Oudhia, D. E. Mager and R. M. Straubinger, *Pharmaceutics*, 2014, **6**, 137.

51 J. M. Metselaar and T. Lammers, *Drug Delivery Transl. Res.*, 2020, **10**, 721.

52 E. K. H. Chow and D. Ho, *Sci. Transl. Med.*, 2013, **5**, 216.

53 J. C. Larsson, C. Vogt, W. Vågberg, M. S. Toprak, J. Dzieran, M. Arsenian-Henriksson and H. M. Hertz, *Phys. Med. Biol.*, 2018, **63**, 164001.

54 D. Clases and R. Gonzalez de Vega, *Anal. Bioanal. Chem.*, 2022, **414**, 7363.

55 Q. Chen, L. Yuan, W.-C. Chou, Y.-H. Cheng, C. He, N. A. Monteiro-Riviere, J. E. Riviere and Z. Lin, *ACS Nano*, 2023, **17**(20), 19810.

56 H. M. Hertz, J. C. Larsson, U. Lundström, D. H. Larsson and C. Vogt, *Opt. Lett.*, 2014, **39**, 2790.

57 K. Shaker, C. Vogt, Y. Katsu-Jimenez, R. V. Kuiper, K. Andersson, Y. Li, J. C. Larsson, A. Rodriguez-Garcia, M. S. Toprak, M. Arsenian-Henriksson and H. M. Hertz, *IEEE Trans. Med. Imaging*, 2020, **39**, 3910.